Supercritical fluid flow dynamics and mixing in gas-centered liquid-swirl coaxial injectors

Liwei Zhang, Xingjian Wang, Yixing Li, Shiang-Ting Yeh, and Vigor Yang

Citation: Physics of Fluids **30**, 075106 (2018); doi: 10.1063/1.5026786
View online: https://doi.org/10.1063/1.5026786
View Table of Contents: http://aip.scitation.org/toc/phf/30/7
Published by the American Institute of Physics

Supercritical fluid flow dynamics and mixing in gas-centered liquid-swirl coaxial injectors

Liwei Zhang, Xingjian Wang, Yixing Li, Shiang-Ting Yeh, and Vigor Yang[a)]
Daniel Guggenheim School of Aerospace Engineering, Georgia Institute of Technology, Atlanta, Georgia 30332, USA

(Received 23 February 2018; accepted 26 June 2018; published online 20 July 2018)

Gas-centered, liquid-swirl coaxial injectors similar to those used in the main chambers of oxidizer-rich staged-combustion engines are investigated computationally, in terms of supercritical fluid flow dynamics and mixing. Gaseous oxygen (GOX) is axially directed through a center post at a temperature of 687.7 K. Kerosene is tangentially introduced into the outer coaxial swirler at a temperature of 492.2 K. The mean chamber pressure of 253.0 bars substantially exceeds the thermodynamic critical pressures of oxygen and kerosene. The end of the GOX post is recessed from the entrance of the taper region, which is connected downstream to an open domain. A wide range of recess lengths (and correspondingly, fuel shielding collar lengths) is considered to determine the dependence of flow characteristics on this geometric parameter. Special attention is given to the regions downstream of the GOX post end and in the taper section, where primary mixing occurs. Instantaneous and time-averaged flow properties, as well as mixing effectiveness, are examined. Results indicate that the recess length plays a critical role in determining the flow evolution and mixing behaviors. In a fully recessed injector without fuel shielding, the initial kerosene/GOX interaction resembles a swirling transverse jet into a crossflow, and flow recirculation occurs near the kerosene injection slit and the head end. In other injectors with fuel shielding, the kerosene flow is predominantly axial before it enters the mixing zone; the coflow kerosene and GOX streams expand radially and recirculate in the wake of the GOX post. Flow unsteadiness arising from the fluid injection and mixing and vorticity production in the boundary layer of the GOX stream, along the wall of the fuel passage, and at the kerosene/GOX interface cause the development of salient vortical structures in the downstream flowfield. The geometric changes at the entrance of the taper region and at the injector exit further alter the flow dynamics, inducing multiple toroidal recirculation zones and secondary vortex structures. *Published by AIP Publishing.*
https://doi.org/10.1063/1.5026786

I. INTRODUCTION

Supercritical fluid flow dynamics and mixing have recently received increased attention due to their broad relevance to science and engineering systems. As the environmental pressure approaches or exceeds the critical points of the working fluids, the underlying flow physics become quite intricate due to thermodynamic nonidealities and transport anomalies in the transcritical regime.[1] Modeling of these problems is severely challenged by the highly nonlinear source terms arising from compressibility effects (volumetric changes induced by changes in pressure) and variable inertia effects (volumetric changes induced by variable composition and/or heat addition).[2] The widely disparate time and length scales involved also impose stringent requirements on numerical simulation algorithms, computing resources, and post-processing of results.[3,4]

The present work investigates supercritical fluid flow dynamics and mixing in a gas-centered liquid-swirl coaxial (GCLSC) injector, as shown schematically in Fig. 1. This type of injector is extensively used in liquid rocket engines,[5] such as the main combustion chambers of the RD-8, RD-170, and RD-180 staged-combustion cycle engines, which have oxygen-rich preburners.[6–8] GCLSC injectors offer excellent combustion efficiency and stability behaviors and relatively simple configurations. Although these engines and their constituent injectors have been in service for decades, performance assessment and in-depth understanding of their fundamental mechanisms remain limited in the open literature, especially for practical operating conditions.

Table I lists the operating conditions of recent studies on GCLSC injectors. Soller *et al.*[9] investigated the combustion stability characteristics in a subscale test facility. They found that the recess length L_r, defined as the distance between the end of the central post and the entrance of the taper region (or the entrance of the combustion chamber, if no taper is considered), plays a critical role in determining the acoustic dynamics of the chamber. Miller *et al.*[10] studied combustion dynamics by changing the combustor length. Lightfoot *et al.*[11] examined the spray behaviors of injectors with different mixing cups and identified flow nonuniformities caused by disturbances in the upstream region. Schumaker *et al.*[12] found negligible impact of the mixing cup length on the liquid film thickness for the gas-to-liquid momentum flux ratio, J, over 400. Im *et al.*[13] compared the spray characteristics in a GCLSC injector and a liquid-centered, gas-swirl coaxial (LCGSC) injector, over

a)vigor.yang@aerospace.gatech.edu

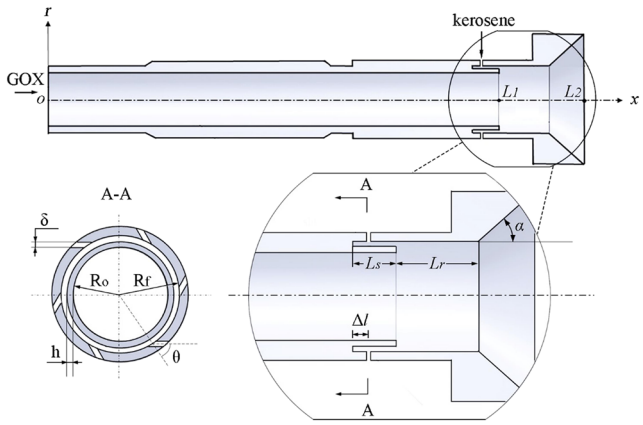

R_0	h	R_f	θ	δ	L_1	L_2	L_s	L_r	Δl	α
5.6	0.7	7.0	63.4°	0.69	93.0	113.1	5.5	10.5	2.0	42°

Units in *mm*, unless stated otherwise.

FIG. 1. Schematic of the GCLSC injector with gaseous oxygen and liquid kerosene as propellants.

a wide range of J. The spray angle was found to decrease with increasing J for the LCGSC injector, while the angle for the GCLSC injector initially decreases at relatively low J, but the trend is reversed with high J. Kulkarni *et al.*[14] examined un-recessed GCLSC injectors.

In the experimental study of Jeon *et al.*,[15] it was noted that as the recess length increased, both the spray cone angle and the droplet size decreased. Schumaker *et al.*[16] found that the swirl strength had little effect on the intact liquid film length but affected the film unsteadiness and gas entrainment, and the injector inlet geometry could change the film thickness. In a numerical study, Trask *et al.*[17] took into account fluid compressibility in an Eulerian two-phase model and captured the sudden flow expansion. Kim *et al.*[18] explored spray patterns at both atmospheric and elevated pressures with different recess lengths and momentum flux ratios. Under high-pressure conditions, an injector with a shorter recess was found to require a higher momentum flux ratio to achieve a spray pattern and mixing similar to that of an injector with a longer recess. Matas *et al.*[19] performed both experimental work and theoretical work. They observed that the intact liquid length decreased as the swirl strength decreased and J increased. The flow oscillation frequencies in the liquid were related to viscous shear instabilities that occurred when an abrupt change in viscosity was present across the interface. Sisco *et al.*[20] examined multiple oxidizer tube lengths and inlet types and found that they had a strong influence on the pressure oscillation in the oxidizer tube of the GCLSC injector. Morgan *et al.*[21] evaluated combustion instabilities using GCLSC injectors as the driving element to produce self-excited oscillations in both longitudinal and transverse chambers. Park *et al.*[22] generated perturbations in the gaseous flow and examined the ensuing instability in the liquid flow. The spray pattern varied over a frequency range of 0.2-1.1 kHz, and the film thickness had a high gain value at both low and high frequencies due to the resonance between the gas feed line and the gas-liquid interface instability. The gain further increased as the momentum flux ratio and recess length increased due to momentum transfer but decreased as the center post thickness decreased due to reduced vortex size.

Many of the existing studies on GCLSC injector flow dynamics were performed with water and air/nitrogen as working fluids under atmospheric conditions, without consideration of the effects of the elevated pressure encountered in operational engines. As observed by Kim *et al.*,[18] however, the flow and mixing behaviors vary noticeably at high pressures. The present study aims to investigate the flow dynamics and mixing effectiveness of a GCLSC injector under supercritical conditions. The chamber pressure substantially exceeds the thermodynamic critical point of the fluid in order to mimic the situations in practical rocket engines. The effect of recess length L_r on the injector evolution[23,24] is examined. The paper is organized as follows. Section II summarizes the

TABLE I. Studies on Gas-Centered, Liquid-Swirl Coaxial (GCLSC) injectors. GOX: gaseous oxygen; MR: mixture ratio; J: gas-to-liquid momentum flux ratio.

References	Fluids	Cold or reacting CFD or experiment	Chamber pressure
Soller *et al.*[9]	GOX/kerosene	Reacting, expt.	40–85 bars
Miller *et al.*[10]	Superheated water and GOX/kerosene	Reacting, expt.	21–24 bars
Lightfoot *et al.*[11]	N_2/water	Cold, expt.	Atmospheric
Schumaker *et al.*[12]	N_2/water	Cold, expt.	Atmospheric
Im *et al.*[13]	Air/water	Cold, expt.	Atmospheric
Kulkarni *et al.*[14]	Air/water	Cold, expt.	Atmospheric
Jeon *et al.*[15]	N_2/water	Cold, expt.	Atmospheric
Schummaker *et al.*[16]	N_2/water	Cold, expt.	Atmospheric
Trask *et al.*[17]	N_2/water	Cold, expt. and 2D CFD	Atmospheric
Kim *et al.*[18]	N_2/water	Cold, expt.	Atmospheric and 59 bars
Matas *et al.*[19]	Air/water	Cold, expt. and theoretical	Atmospheric
Sisco *et al.*[20]	Decomposed H_2O_2/JP-8	Reacting, expt.	28 bars
Morgan *et al.*[21]	Decomposed H_2O_2/RP-1	Reacting, expt. and CFD	8–10 bars
Park *et al.*[22]	Air/water	Cold, expt.	Atmospheric

theoretical formulation and numerical method for treating real fluid dynamics. Section III describes the injector configuration, operating conditions, and boundary conditions. Section IV presents the results and discussion of injector flow dynamics and mixing characteristics. Conclusions are drawn in Sec. V.

II. THEORETICAL FORMULATION AND NUMERICAL METHOD

The basis of the present study is the integrated theoretical/numerical framework detailed in Refs. 3 and 25 for treating real-fluid dynamics over a complete range of fluid thermodynamic states, from ideal gas to compressed liquid. The formulation is based on the Favre-averaged conservation equations of mass, momentum, energy, and species concentrations for a compressible, multicomponent system. Turbulence closure is achieved by means of large-eddy-simulation (LES) techniques, with subgrid-scale motions treated by a compressible Smagorinsky model.[26] Thermodynamic properties are determined using the concepts of partial-mass and partial-density properties,[1,3] along with a modified Soave-Redlich-Kwong equation of state. Transport properties are evaluated with extended corresponding-state principles.[1] A three-component surrogate consisting of n-decane, n-propylbenzene, and n-propylcyclohexane (74/15/11 by mole fraction) is used to calculate the physicochemical properties of kerosene.[27]

To tackle the numerical stiffness arising from steep gradients of flow properties and wide disparities of characteristic time and length scales, a unified treatment of general fluid thermodynamics is established and incorporated into a preconditioning scheme.[3,28] All the numerical properties, including the preconditioning matrix, Jacobian matrices, and eigenvalues, are derived directly from fundamental thermodynamics theories, rendering a self-consistent and robust algorithm. This methodology can accommodate any equation of state and is valid for fluid flows at all speeds and all fluid thermodynamic states of concern.

Boundary conditions are treated based on the method of characteristics.[29] The governing equations and associated boundary conditions are solved using a density-based, finite-volume approach, along with a dual time-step integration technique.[30] The convective fluxes are evaluated by a fourth-order central difference scheme in generalized coordinates. A sixth-order scalar dissipation scheme is employed to suppress numerical oscillations. The dissipation coefficient is set to be 0.001 to minimize contamination from numerical dissipation. Such a spatial discretization strategy satisfies the total-variation-diminishing condition and ensures computational stability.[31] Temporal integration is achieved by a second-order backward difference, and the inner-loop pseudo-time term is integrated with a four-step Runge-Kutta scheme. The numerical scheme is parallelized by a message-passing-interface technique to enhance computational efficiency.

III. PHYSICAL CONFIGURATION AND OPERATING CONDITIONS

Figure 1 shows schematically the physical model of concern, which is similar to the main combustor injectors employed in the oxygen-rich, staged-combustion engines RD-170 and RD-180.[7,8] High-temperature gaseous oxygen (GOX) is delivered to the center cylindrical tube, known as the GOX post, and mixed with liquid kerosene injected tangentially into the outer annulus. The origin of the coordinates is located at the center of the entrance of the GOX post, which measures 11.2 mm in diameter, D_o, 0.7 mm in thickness, h, and 93.0 mm in length, L_1, in the baseline design. The outer annular fuel passage has a width, ξ, of 0.7 mm. The injector is equipped with a total of 12 tangential fuel ports, and each has a diameter, D_i, of 1.2 mm. In the present study, these fuel ports are simplified by a single circular injection slit located 2.0 mm from the head end of the fuel passage. The tangential injection angle, θ, is 63.4°, and the circular slit has a width, $\delta = 12\pi(0.5D_i)^2/2\pi R_f \cos\theta$, of 0.69 mm. The length of the collar that shields the fuel from the oxidizer is treated as a variable in the parametric study. The mixing cup starts from the GOX post exit and has a diameter, $D_f = D_o + 2h + 2\xi$, of 14.1 mm. It is connected downstream with a taper region having a divergence angle, α, of 42° and a length, L_t, of 9.6 mm. The exit diameter, D_t, is 31.4 mm. The injector is exposed to an open domain, which computationally spans 90.0 mm in the radial direction, D_c, and 158.0 mm in the axial direction, L_c.

The length of the recess region, L_r, from the GOX post exit to the taper entrance is an important factor in determining injector performance.[24,32–34] In the present study, the recess length is varied from 0 to 16.0 mm, corresponding to the change in the length of the fuel shielding collar L_s from 16.0 to 0 mm. The mixing cup has a length, $L_m = L_r + L_t$, of 20.1 mm in the baseline design. The total length of the injector element, $L_2 = L_1 + L_r + L_t$, remains fixed at 113.1 mm. Table II lists the lengths of the fuel annulus, GOX post, and recess for the six cases considered in the present study, as well as the corresponding recess number, defined as the ratio of the recess length to the radius of the injector at the entrance of the mixing cup, $N_r = L_r/R_i$.

The injector operating pressure is 253.0 bars, identical to the main combustor pressure of the RD170/180 engines. Note that the critical pressure and temperature are 50.8 bars and 154.8 K for oxygen and 18.2 bars and 658.2 K for dodecane, respectively. Table III lists the flow conditions.

TABLE II. Length of fuel passage, oxidizer post, and recess.

	Case 1	Case 2	Case 3[a]	Case 4	Case 5	Case 6
L_s (mm)	0	3.0	5.5	9.0	12.5	16.0
L_1 (mm)	87.5	90.5	93.0	96.5	100.0	103.5
L_r (mm)	16.0	13.0	10.5	7.0	3.5	0
N_r	2.3	1.8	1.5	1.0	0.5	0

[a]Baseline design.

TABLE III. Flow conditions.

	Oxidizer	Fuel
Fluid	GOX	Kerosene
Mass flow rate (kg/s)	1.33	0.48
Temperature (K)	687.7	492.2
Pressure (bar)	253.0	253.0
Density (kg/m^3)	131.4	640.8

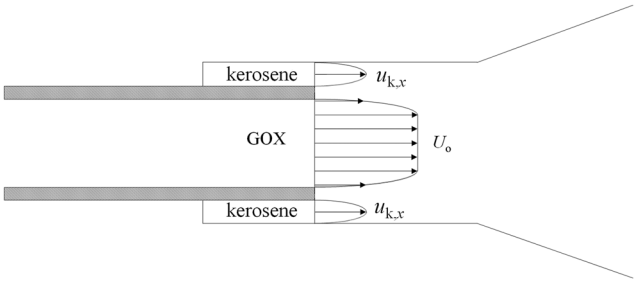

FIG. 2. Schematic of the flowfield in the mixing zone.

The nominal oxidizer-to-fuel momentum flux ratio is estimated as $J = \rho_o U_o^2 / \rho_f U_f^2$. The reference velocity for GOX is calculated from the GOX mass flow rate and passage cross-sectional area, 102.0 m/s. The reference velocity of kerosene needs to be evaluated carefully. For case 1, without shielding, kerosene is tangentially introduced into the injector; U_f is taken as the radial velocity component at the injection slit, 24.5 m/s. For other cases with shielding, U_f is calculated from the kerosene mass flow rate and fuel passage cross-sectional area, 26.6 m/s. J is thus obtained as 3.5 for case 1 and 3.0 for cases 2-6. Figure 2 shows schematically the time-averaged axial velocity profile at the mixing cup entrance (that is, the GOX post exit).

Only a cylindrical sector of the injector is considered in the simulations, with periodic boundary conditions specified in the azimuthal direction. At the GOX and kerosene entrances, an acoustically non-reflecting boundary condition is implemented.[29] At the downstream boundary of the computational domain, sponge layers are employed in both the axial and radial directions to prevent the reflection of unsupported flow features.[35] All solid walls are assumed to be adiabatic, and no-slip conditions are enforced.

IV. RESULTS AND DISCUSSION

The theoretical/numerical framework has previously been validated against a variety of supercritical fluid flow problems.[2,3,25,36,37] To minimize numerical uncertainty, a grid-convergence study was performed for case 3 (the baseline case). Three different grid levels were considered, with a

TABLE IV. Numerical grid matrices.

	GOX post	Fuel passage	Mixing cup	Downstream	Total cell number
Level 1	224×64	56×24	160×112	160×160	0.58×10^5
Level 2	448×128	122×48	320×224	320×320	2.31×10^5
Level 3	896×256	224×6	640×448	640×640	9.26×10^5

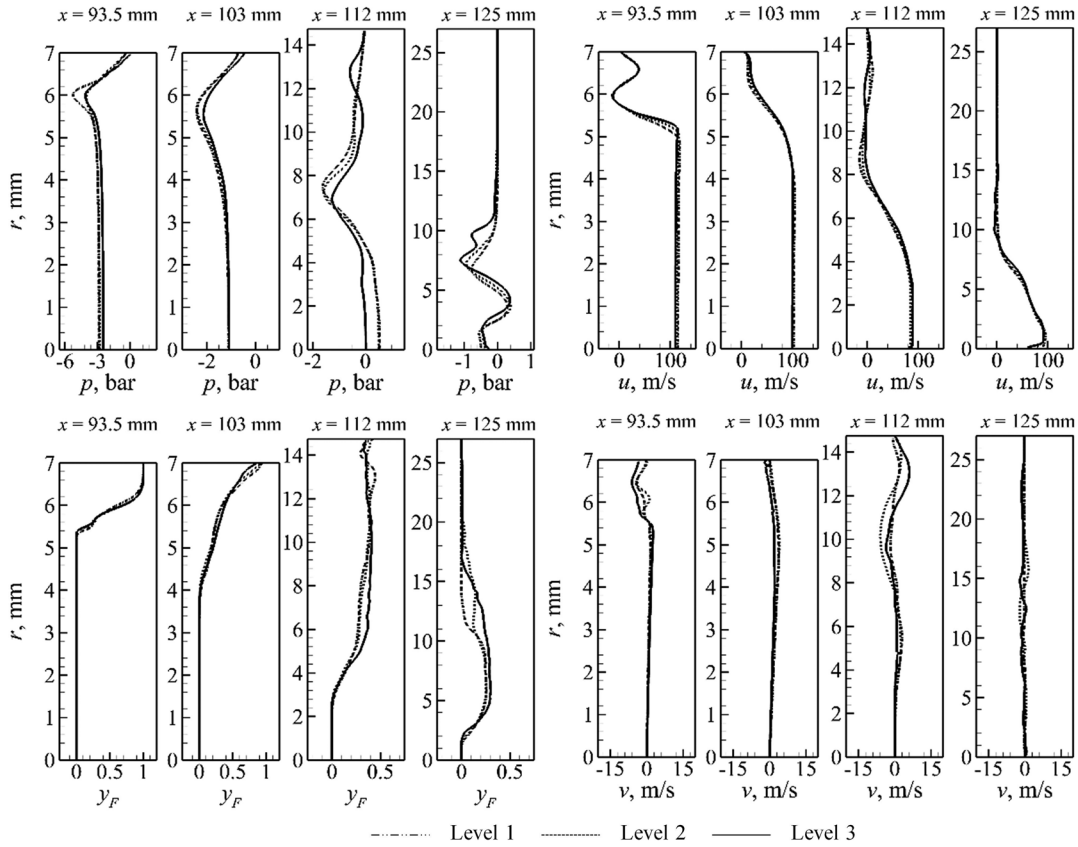

FIG. 3. Effect of grid resolution on radial distributions of mean gauge pressure, kerosene mass fraction, and axial and radial velocity components at different axial locations for three different grid levels (case 3).

refinement ratio of two in each direction. Table IV summarizes the numbers of finite-volume cells in the GOX post, fuel passage, mixing cup, and downstream domain. The grid points are clustered in regions with stiff flow gradients and toward the walls to adequately treat boundary layers. The Reynolds number based on the width of the fuel annulus ξ and kerosene properties is

$$Re_\xi = \frac{\rho_f U_f \xi}{\mu_f} = 4.14 \times 10^4. \quad (1)$$

The corresponding Kolmogorov and Taylor scales are

$$\eta = \xi \cdot Re_\xi^{-3/4} = 0.24\ \mu\text{m}, \quad (2)$$

$$\lambda = \sqrt{10}\xi \cdot Re_\xi^{-1/2} = 10.88\ \mu\text{m}. \quad (3)$$

The intermediate level 2 grid has a grid size of 5 μm near the injector wall in the mixing cup and 10 μm near the fuel shielding collar rim in the radial direction. Both sizes are comparable with the Taylor microscale and fall in the inertial

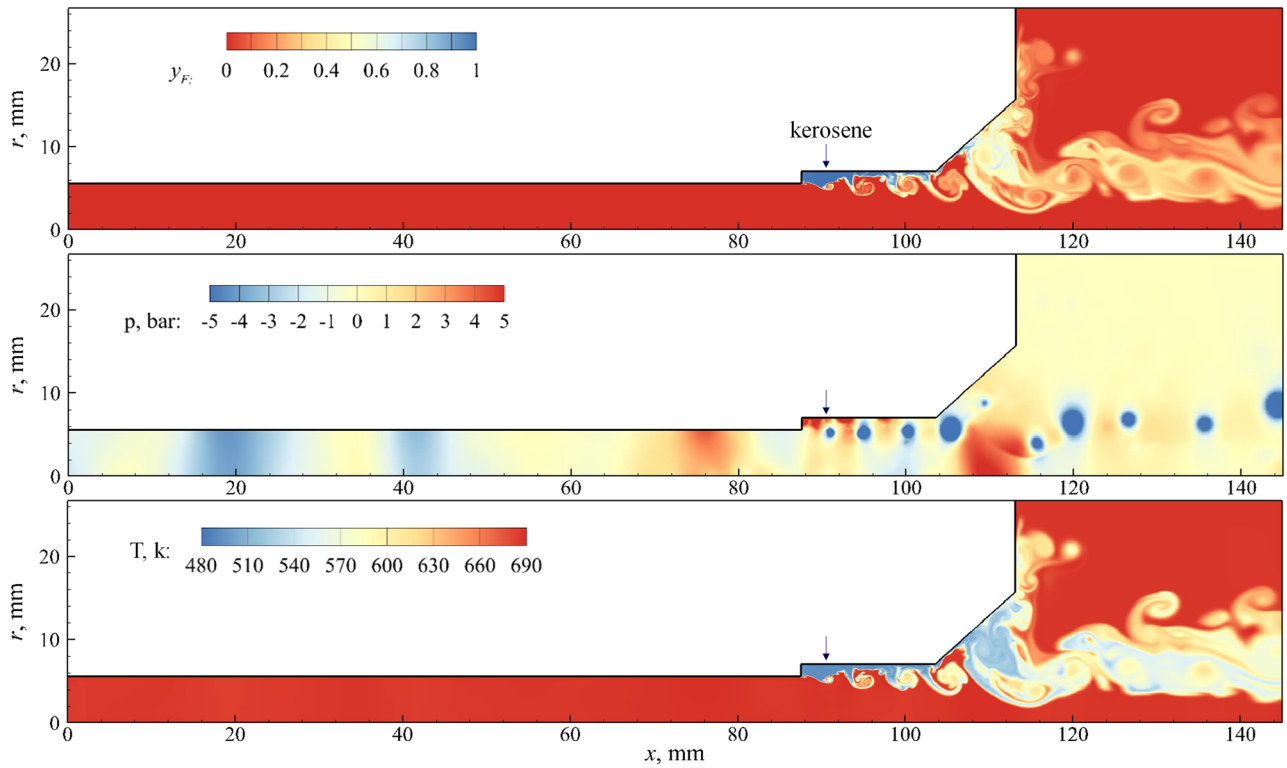

FIG. 4. Snapshots of kerosene mass fraction, gauge pressure, and temperature fields at t = 15.0 ms (case 1).

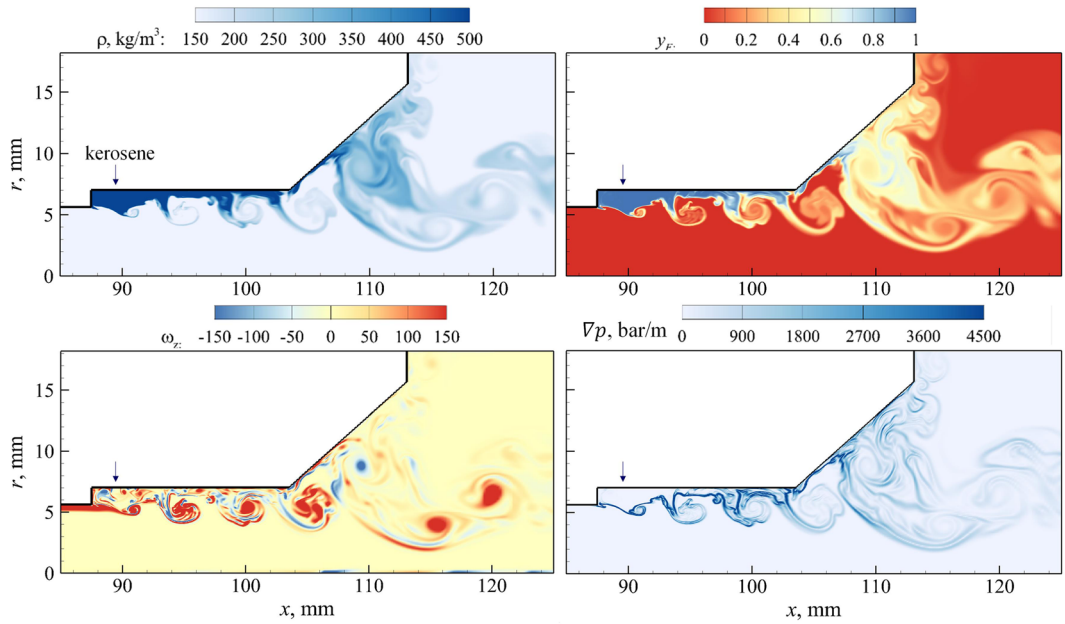

FIG. 5. Snapshots of density, kerosene mass fraction, vorticity, and pressure-gradient fields at t = 15.0 ms (case 1).

subrange of the turbulent kinetic energy spectrum estimated by the Kolmogorov-Obukhov theory.

Figure 3 compares the radial distributions of the mean gauge pressure, kerosene mass fraction, and axial and radial velocity components at different axial locations for the three different grid levels for case 3. The reference pressure is set as 253.0 bars. Good agreement is observed among the mean profiles, except at x = 112 mm in the taper section and x = 125 mm at the injector exit, where a sudden geometric change induces strong flow distortions (as discussed in Sec. IV B). The discrepancy in the fuel mass fraction at these regions is especially apparent because of the unsteady mixing process, which is not fully captured by the LES calculations. In consideration of computational accuracy and efficiency, the intermediate grid, level 2, is selected for the computations in the present study. The time step is fixed at 2.0×10^{-7} s for temporal accuracy. The local Courant-Friedrichs-Lewy number varies in the range of 0.1-0.5, depending on local flow velocities and grid sizes.

A. Injector flow dynamics

For all of the cases, calculations are initiated by delivering the GOX flow through the injector at prespecified conditions at t = 0. Kerosene injection is activated at t = 9.0 ms, after the GOX flow has completed its transient stage. The flowfield reaches its stationary state at around t = 12.0 ms, when the kerosene/GOX mixing field is fully established. Figure 4 shows the instantaneous fields of kerosene mass fraction, gauge pressure, and temperature at t = 15.0 ms for case 1 (no kerosene fuel shielding). Figure 5 shows the corresponding distributions of density, kerosene mass fraction, vorticity, and pressure gradient in the mixing zone. High-speed, high-temperature GOX flows through the center post, and low-speed, high-density kerosene is discharged from the tangential

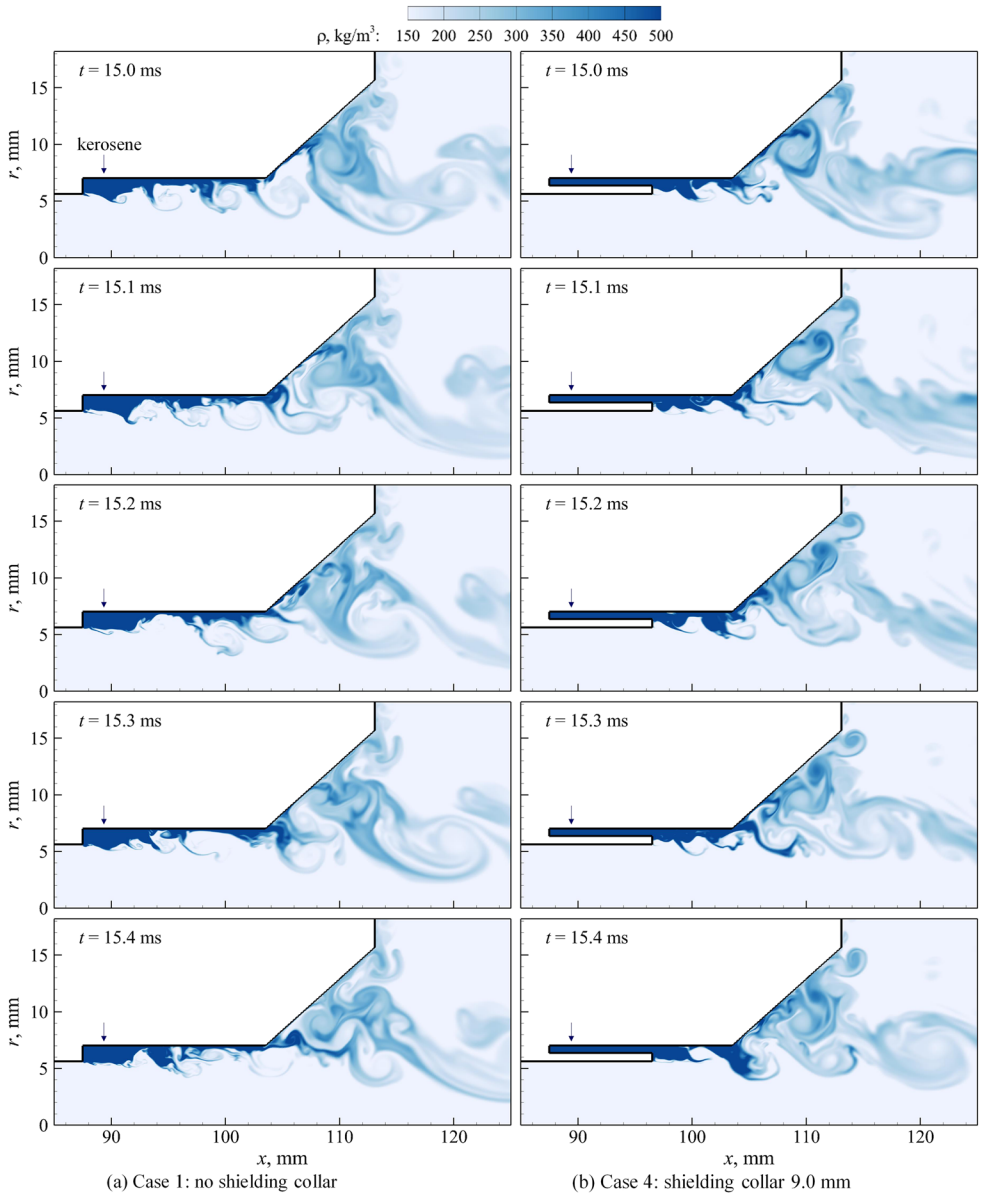

(a) Case 1: no shielding collar (b) Case 4: shielding collar 9.0 mm

FIG. 6. Temporal evolution of the density field in the mixing section.

entry, producing complicated flow structures in the mixing zone. The injector wall confines the shear layer before the entrance to the taper section. This type of configuration often generates absolute instability and may induce self-sustained global instabilities.[38] Kerosene mixes rapidly with GOX while traveling downstream and forms large-scale structures. The intricate interactions among fluid injection, mixing, and acoustic resonance induce well-defined pressure oscillations in the GOX post, which gradually lose regularity in the downstream region due to viscous damping and turbulent diffusion.

In Secs. IV A 1–IV A 4, the flowfield is analyzed in detail to characterize the mixing layer development. Special attention is given to the region near the GOX post exit to identify the formation and initial spreading of the mixing layer.

1. Density field

Figure 6 shows the evolution of the density field in the mixing zone for cases 1 and 4, and Fig. 7 shows the corresponding close-up views near the GOX post exit. At the entrance of the mixing cup, a kerosene film forms along the injector wall because of the swirl-induced centrifugal force. The interface between the low-speed kerosene and the high-speed GOX is intrinsically unstable and features hydrodynamic instability waves.[37] A short distance downstream of the post exit, the longitudinal mode of the hydrodynamic instability grows, forming large-scale billows as the interface moves toward the taper section. Since the GOX stream travels faster than kerosene, the velocity gradient leads to momentum transfer and shear stress on the interface. The resultant vorticity (shown in Figs. 10 and 11) in the azimuthal direction induces counterclockwise-rotating roll-ups in the mixing layer. As these forward-rolling vortices travel downstream, they grow in size and the spacing between successive vortices increases. In case 1, the vortices are well structured and measure up to 3 mm in diameter before they enter the taper. The traveling speed of the vortices, based on the core locations, is estimated to be 60 m/s, approximately equal to the average of the GOX and kerosene speeds, and consistent with classical mixing layer theories.[39] In case 4, the kerosene film appears thicker, and the vortices are smaller and less coherent, mainly because of a shorter travel distance.

In a swirling flow, there is a radially outward centrifugal force acting on the mass ($f \sim mu_\theta^2/r$). In order to move the mass closer to the axis (say from r_1 to r_2, where $r_1 = r_2 + \Delta r$ and Δr has an infinitesimal positive value), work must be done, and hence, the mass gains potential as it moves inwards,

$$W = -\int_{r_1}^{r_2} f dr = -\int_{r_1}^{r_2} \frac{mu_\theta^2}{r} dr = m\bar{u}_\theta^2 \cdot \ln\left(\frac{r_1}{r_2}\right) > 0. \quad (4)$$

Note that kerosene has a substantially larger density than GOX. When a disturbance moves a small amount of kerosene inwards, displacing an equal volume of GOX outwards, a mass

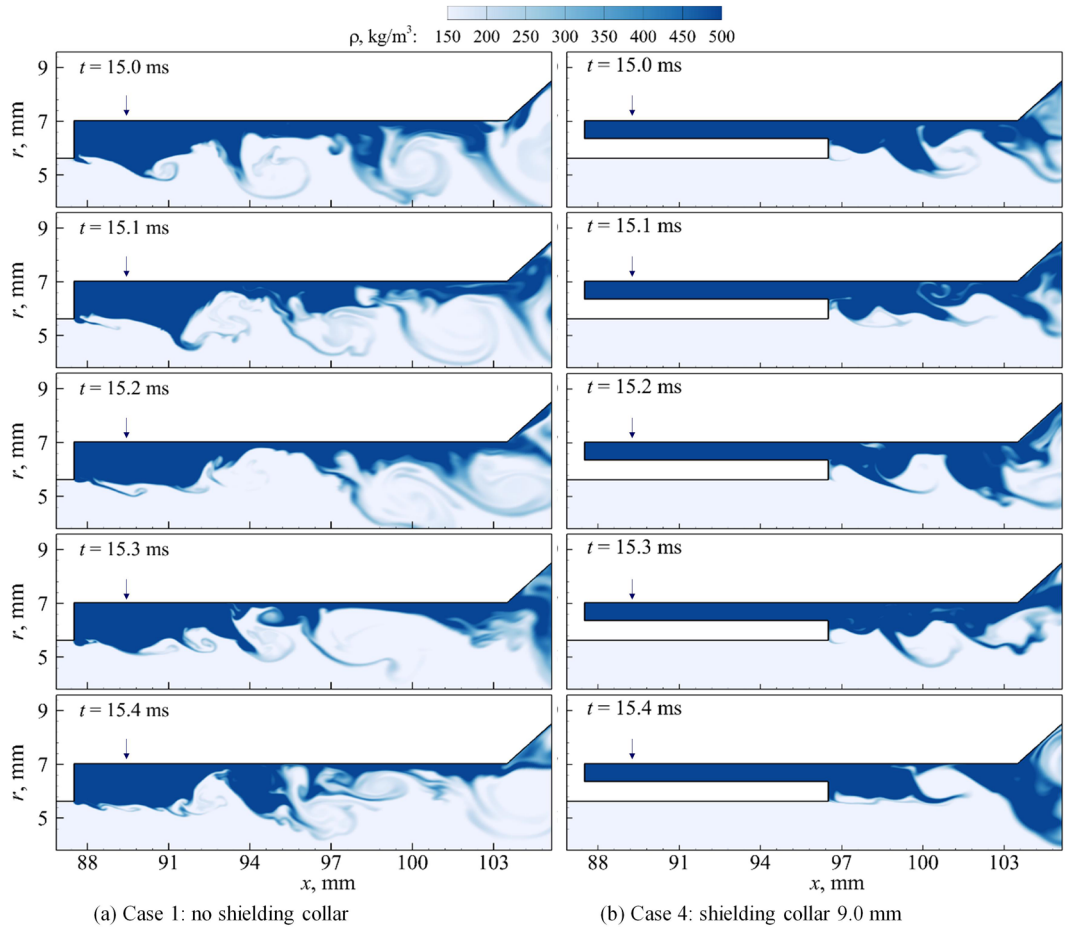

(a) Case 1: no shielding collar (b) Case 4: shielding collar 9.0 mm

FIG. 7. Temporal evolution of the density field near the GOX post exit.

has been moved toward the axis. Therefore, the combined potential energy of the flow increases, and the disturbance will diminish and revert back to the original equilibrium state of the system—an inverse of the development of Rayleigh-Taylor instabilities. This eliminates the contribution of the density gradient to the mixing layer development in the present study.

2. Kerosene mass-fraction field

Figure 8 shows the evolution of the kerosene mass-fraction field in the mixing zone for cases 1 and 4. The isolines show the kerosene mass fraction of 0.4 (dashed lines) and 0.6 (solid lines). The unsteadiness of the kerosene injection and the intrinsic hydrodynamic instabilities in the kerosene/GOX shear layer lead to the formation of large-scale vortices. These structures engulf GOX bulk and draw it into the shear layer (macromixing). They also stretch the interface between the unmixed fluids, increasing the interfacial area and steepening the local concentration gradients, and enhance the diffusive micromixing. As shown in Fig. 8, GOX entrains the kerosene film and macromixing takes place in the early mixing region. As the mixing layer travels downstream, large-scale vortices grow and fine structures emerge, promoting the disintegration and the dispersion of the kerosene stream. This phenomenon is especially prominent in the taper region, and as a result, a sizeable part of the injector has a kerosene mass fraction between 0.4 and 0.6 (also shown in Fig. 16).

Figure 9 shows close-up views of the kerosene mass-fraction field near the GOX post exit. Since kerosene is tangentially introduced into the injector (case 1) or the fuel passage (case 4), the centrifugal force prevents it from penetrating deeply into the injector center. The local kerosene mass faction holds at unity near the wall for both cases. In case 1, the transverse motion of the injected kerosene and the recirculating flow further constrain the fuel to the corner region, and only a slight amount of GOX is observed near the head end. At the GOX post tip, on the other hand, a thin kerosene stream entrains the otherwise smooth GOX flow and rolls up a small volume of GOX as it convects downstream, forming the very early mixing layer. The crest marked by A at the devolved kerosene/GOX interface subsequently increases in size as the GOX flow passing the crest accelerates and decreases the local static pressure. Downstream of $x = 90$ mm, the transverse kerosene stream meets these crests, generating more coherent structures, marked by B, C, and D. In case 4, the rim of the fuel-shielding collar plays an important role in the initialization of the mixing layer. As the outer kerosene and the inner GOX expand immediately downstream of the rim, recirculation occurs behind the rim, and kerosene entrainment takes place. The unsteadiness in the kerosene stream induces strong disruptions on the kerosene/GOX interface, creating large crests and engulfing GOX bulk. This macro-mixing process near the GOX post exit defines the early-stage mixing characteristics and has a significant impact on the subsequent flow development.

3. Vorticity field

Figure 10 shows the evolution of the vorticity field in the mixing zone for cases 1 and 4. The bright red regions mark the

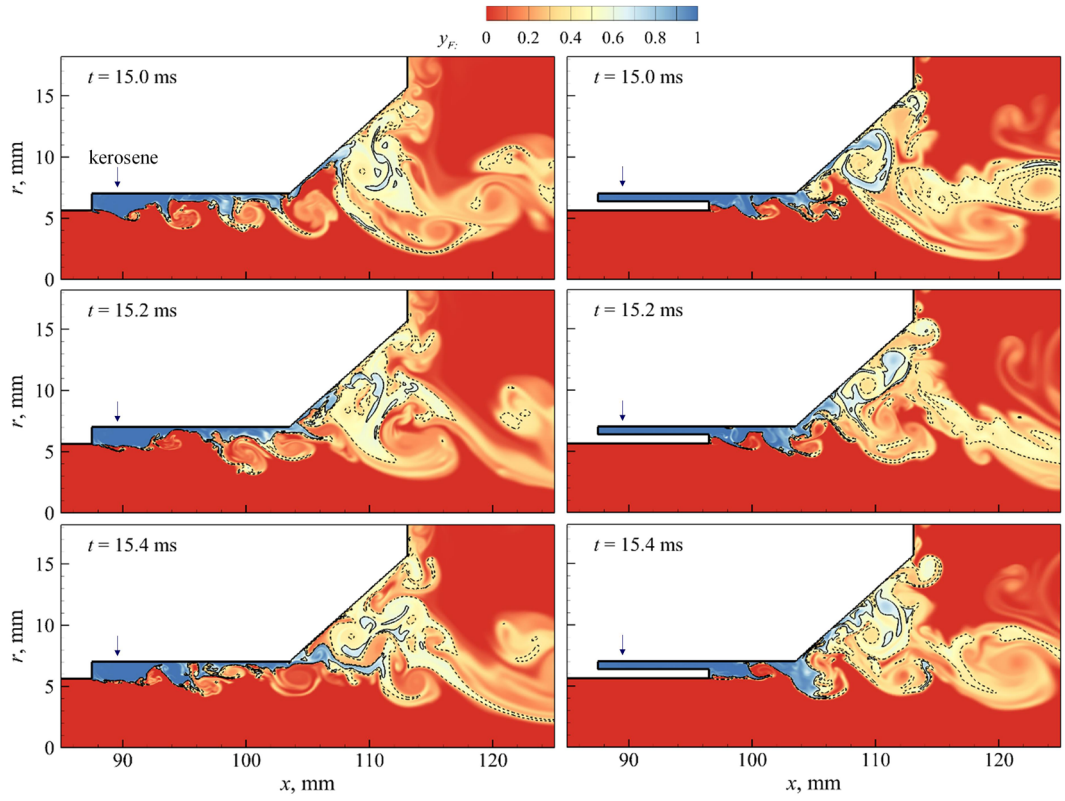

(a) Case 1: no shielding collar (b) Case 4: shielding collar 9.0 mm

FIG. 8. Temporal evolution of kerosene mass fraction in the mixing section.

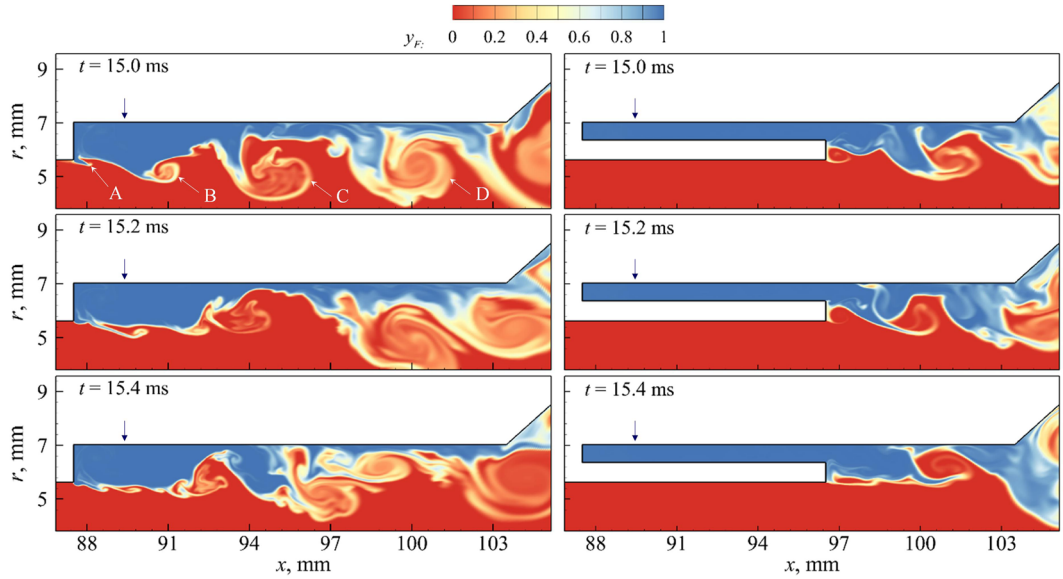

(a) Case 1: no shielding collar (b) Case 4: shielding collar 9.0 mm

FIG. 9. Temporal evolution of kerosene mass fraction near the GOX post exit.

locations of high, positive azimuthal vorticity, mainly generated in the boundary layer of the incoming GOX stream and supplemented by minor production at the kerosene/GOX interface. As positive vorticity continuously sheds from the GOX post tip, a vortex train forms in the mixing cup. A noticeably smaller amount of negative vorticity is produced near the kerosene injection slit in case 1 and along the inner wall of the fuel passage in case 4, as well as in small separation zones at the center. As the kerosene/GOX mixing layer develops, both negative and positive vorticities entangle and disperse, tracing the two streams to some extent. Flow recirculation occurs in the fuel passage for case 4 and in the upstream part of the mixing cup for both cases. Close-up views of instantaneous streamlines are shown near the wall at the taper entrance in Fig. 10(b), visualizing the localized flow separation and reattachment. Once the flow enters the taper region, the coherent

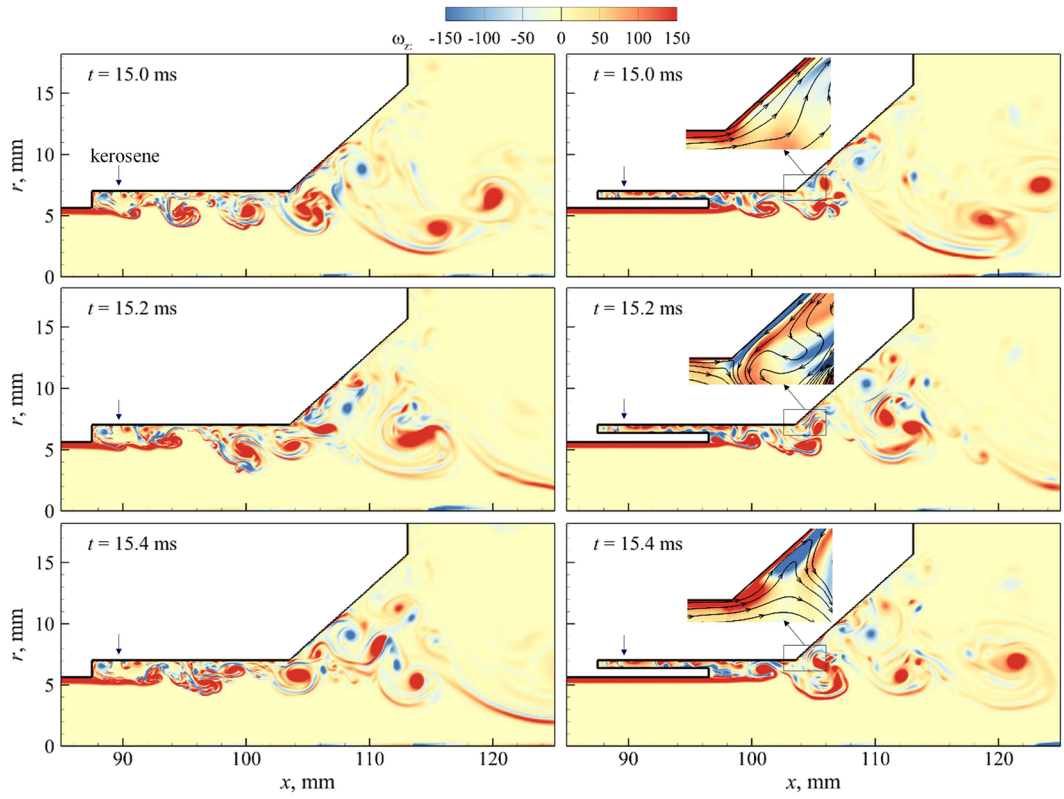

(a) Case 1: no shielding collar (b) Case 4: shielding collar 9.0 mm

FIG. 10. Temporal evolution of vorticity in the mixing section.

vortical structures rapidly enlarge, creating a wide vorticity plume that occupies most of the injector cross sections. The observed behavior results from the flow expansion in the taper section; the flow speed decreases and the vortices also travel slowly. Since the lumps of vorticity persist, the incoming eddies stretch and/or amalgamate into larger structures. Each pairing interaction redistributes vorticity into larger vortices, with a doubled wavelength and halved frequency. Flow recirculation occurs at the taper region and the injector exit, and the sizes and axial locations of the vortices are closely related to their evolution. The time-averaged structures of the recirculating flows are shown in Fig. 14.

Figure 11 shows close-up views of the vorticity distribution in the wake of the GOX post. Also shown are the instantaneous streamlines near the kerosene inlet in case 1 [Fig. 11(c)] and near the collar rim in case 4 [Fig. 11(d)]. In both cases, a large amount of vorticity is generated in the wall boundary of the GOX post. In case 1, the transverse momentum of the kerosene leads to the formation of a small separation zone immediately ahead of the jet, a large recirculation zone in the corner, and an inward flow near the head end. As the GOX travels downstream of the post, it expands radially. The transverse motion of the kerosene jet, however, suppresses such expansion. Early stage GOX entrainment into the kerosene is only possible near the head end, and the axial momentum of the GOX stream deflects the kerosene jet. The two streams meet at x = 90 mm, where significant mixing between GOX and kerosene occurs. A large vortex appears at x = 90.5 mm at t = 15.0 ms.

In case 4, the wall boundaries of the fuel passage provide another source of vorticity. Because of intrinsic flow oscillations, vorticity enters the mixing cup intermittently, forming a wavy vorticity plume downstream of the shielding collar. Both the kerosene and GOX streams expand rapidly when entering the mixing cup, as visualized by the curved vorticity trajectories and the streamlines in Fig. 11(d). The highly unsteady kerosene flow induces the shedding of a series of vortices from the outer collar rim, which subsequently varies the flow direction. Near the collar rim, two counter-rotating recirculating zones are produced, as is typical in the wake flow behind a splitter plate.[40] They are strongly influenced by the incoming streams and constantly change in shape and size. Consequently, the contact point of the main kerosene and GOX streams varies between x = 97.5 and 98.5 mm

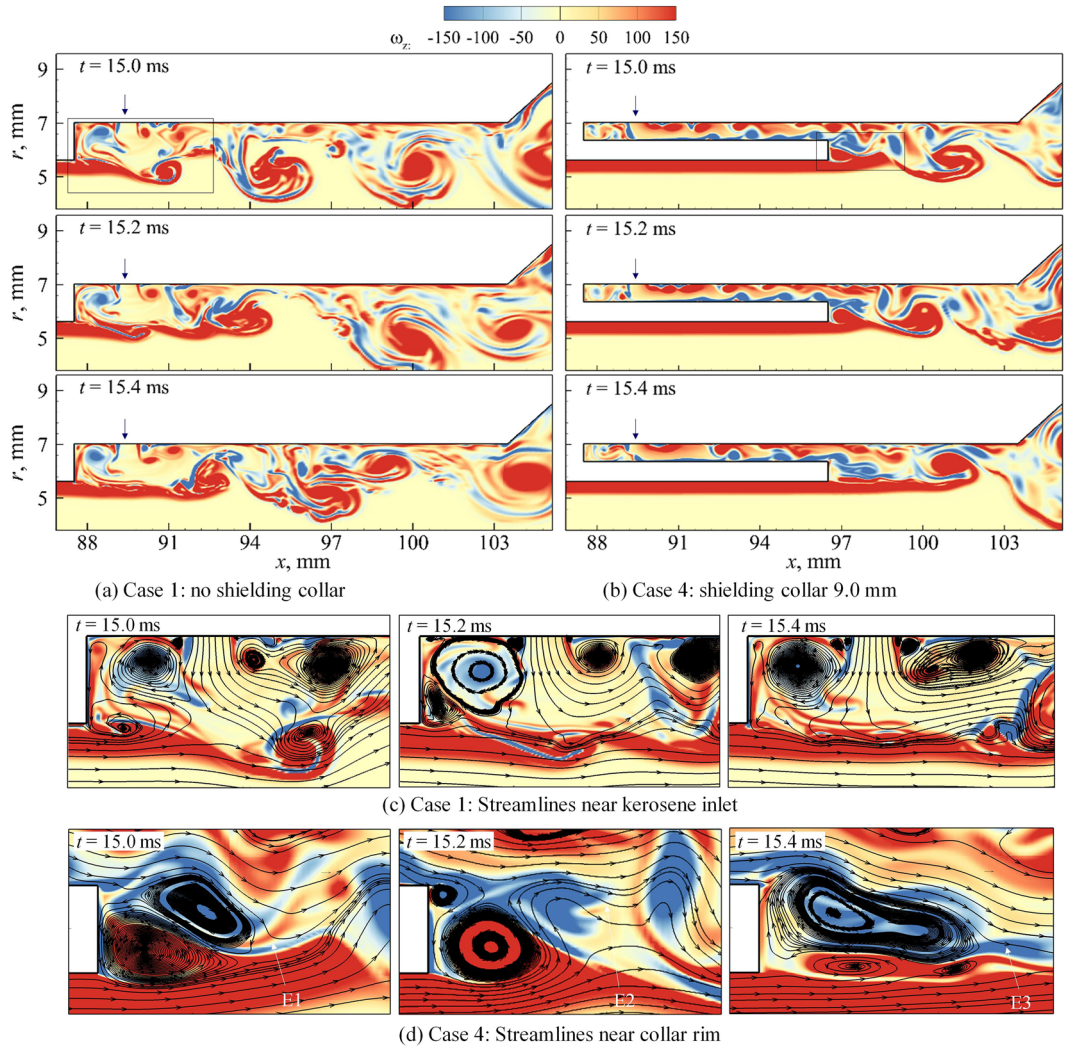

(a) Case 1: no shielding collar

(b) Case 4: shielding collar 9.0 mm

(c) Case 1: Streamlines near kerosene inlet

(d) Case 4: Streamlines near collar rim

FIG. 11. Temporal evolution of vorticity near the GOX post exit and close-up views of streamlines.

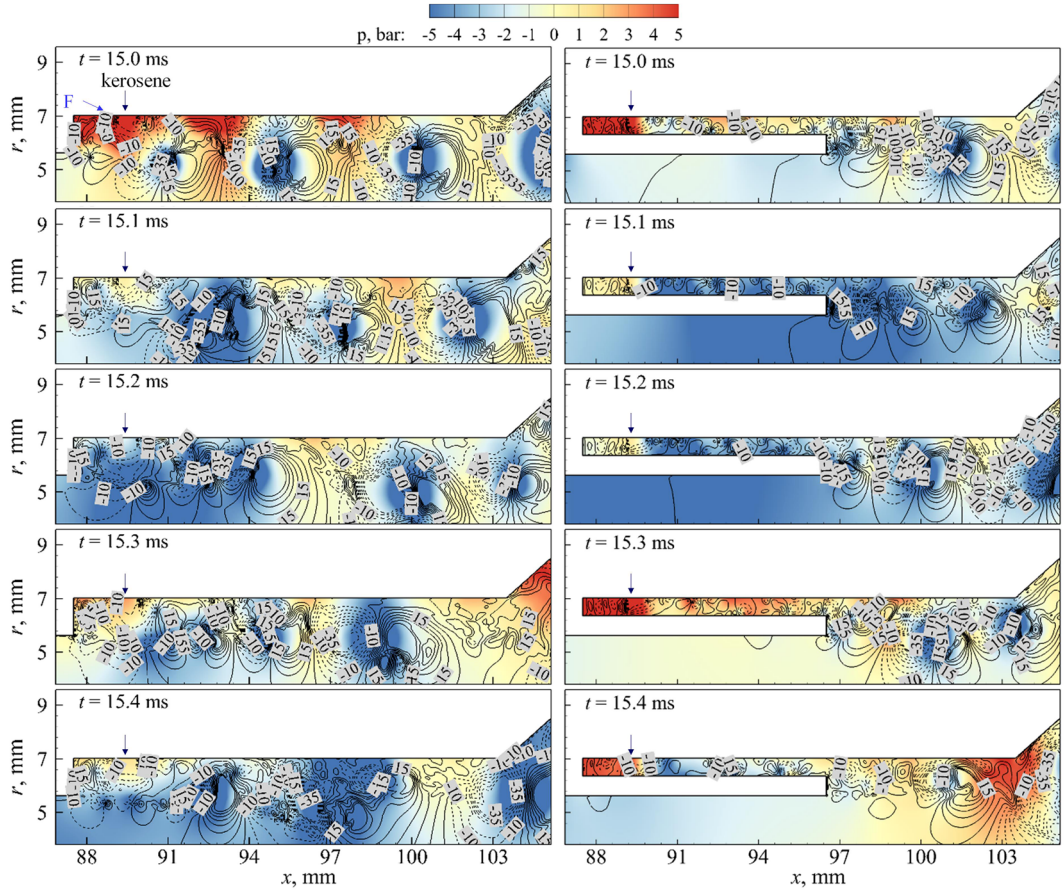

(a) Case 1: no shielding collar (b) Case 4: shielding collar 9.0 mm

FIG. 12. Temporal evolution of the pressure field near the GOX post exit (with radial velocity contours).

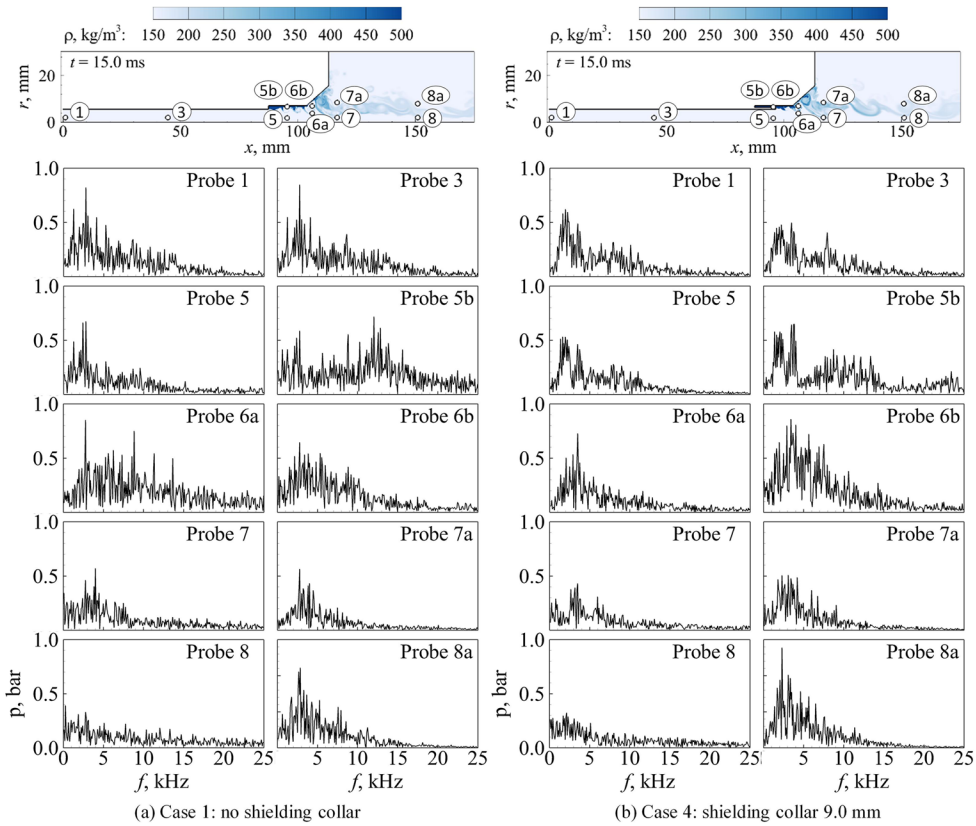

(a) Case 1: no shielding collar (b) Case 4: shielding collar 9.0 mm

FIG. 13. Power spectral densities of pressure fluctuations at different locations.

as marked by E1, E2, and E3. These two streams have distinct velocities, densities, and vorticities, and this leads to dynamic structures in the mixing layer in the downstream region.

4. Pressure field

Figure 12 shows the evolution of gauge pressure with radial velocity isolines near the GOX post exit for cases 1 and 4. The dashed lines denote negative radial velocity. In case 1, the transverse momentum of kerosene causes a negative radial velocity field near the fuel inlet and a time-evolving radial gradient in the pressure field. Pressure in the near-wall region peaks at t = 15.0 ms and decreases to a much lower value at t = 15.2 ms. As the kerosene jet penetrates into the GOX stream, a small separation zone occurs ahead of the injection slit, as suggested by the positive-negative variation of velocity marked by F. The corner flow then moves to the center region, as indicated by the negative radial velocity near the head end. In case 4, since kerosene is first introduced into the fuel passage, where it is shielded by the collar, the flow is predominantly axial before it enters the mixing zone at x = 95.5 mm. Therefore, the pressure field does not exhibit radial gradient; the observed variations are mainly induced by the interaction between the GOX and kerosene flows. Note that since the pressure is slightly higher in the kerosene flow than in the GOX flow, the radial velocity close to the post tip is negative.

The flowfield is extensively probed to characterize its dynamics. Figure 13 shows the locations of measurements and their corresponding power spectral densities (PSD) of pressure for cases 1 and 4. Also shown are instantaneous density fields. Probes 1, 3, and 5 are located within the GOX post, where the acoustic oscillation is primarily longitudinal. The three frequency spectra show almost identical contents. If the region between the entrance of the GOX post and the entrance of the taper section is acoustically treated as a half-wave resonator, its natural frequency is estimated as

$$f = c/2(L + \Delta L), \tag{5}$$

where c is the speed of sound in the GOX stream and L is the combined length of the GOX post and the recess. The correction factor ΔL is taken as $0.6(R_o + R_i)$, where R_o (=5.60 mm) and R_i (=7.05 mm) are the radii of the entrance of the GOX post and the entrance of the taper section, respectively. In the present study, c = 537.82 m/s, L = 103.5 mm, and ΔL = 7.59 mm. The resonance frequency becomes 2.42 kHz, as observed in the plots. Probe 5b is located in the kerosene stream. In addition to the harmonics in the low-frequency regime (f < 5 kHz), intensive oscillations take place around the frequency of 12.5 kHz. This phenomenon is especially obvious in case 1 and can be attributed to the hydrodynamic instability arising from the fuel injection. For case 1, without fuel shielding, the acoustic and hydrodynamic instabilities coexist with noticeable magnitudes at Probes 6a in the taper region. For case 4, with fuel shielding, the Probe 6a data suggest that dominant acoustic oscillations and hydrodynamic instabilities are relatively weak, an indication of the effects of the shielding collar. As the mixture moves downstream and deflects outwards, the region close to the central plane tends to quiet down, as shown from Probes 7 and 8. The mixing zone, however, becomes more oscillatory at frequencies close to those observed within the GOX post. Even though the taper damps the high-frequency oscillations, the dominant acoustic modes still travel downstream and influence the later flowfield.

B. Mean flow properties

The flow characteristics are further examined in the light of time-averaged properties. Figure 14 shows the streamlines in the mixing cup and its downstream region. Close-up views near the GOX post tip are shown in Figs. 14(c) and 14(d). In case 1, the transverse injection of kerosene directly into the injector creates a recirculation zone in the head end, as well as a small area of separation immediately ahead of the injection slit. Because of the small momentum flux ratio between the kerosene and GOX, and swirl-induced centrifugal force, the kerosene stays close to the wall and fills the entire corner region and the near-wall zone. Immediately downstream of the injection slit, the kerosene flow separates and then reattaches to the wall, creating a stagnation point with a locus of positive divergence (node) at x = 90.6 mm; this structure is typical of a transverse jet in crossflow.[41,42] The swirl-induced centrifugal force and the expanding GOX stream push the kerosene toward the wall, as shown by the slightly tilted streamlines between x = 93 and 103.5 mm. As the flow enters the taper region, the geometric change causes flow expansion, and the otherwise smooth streamlines curve upward, forming a small separation

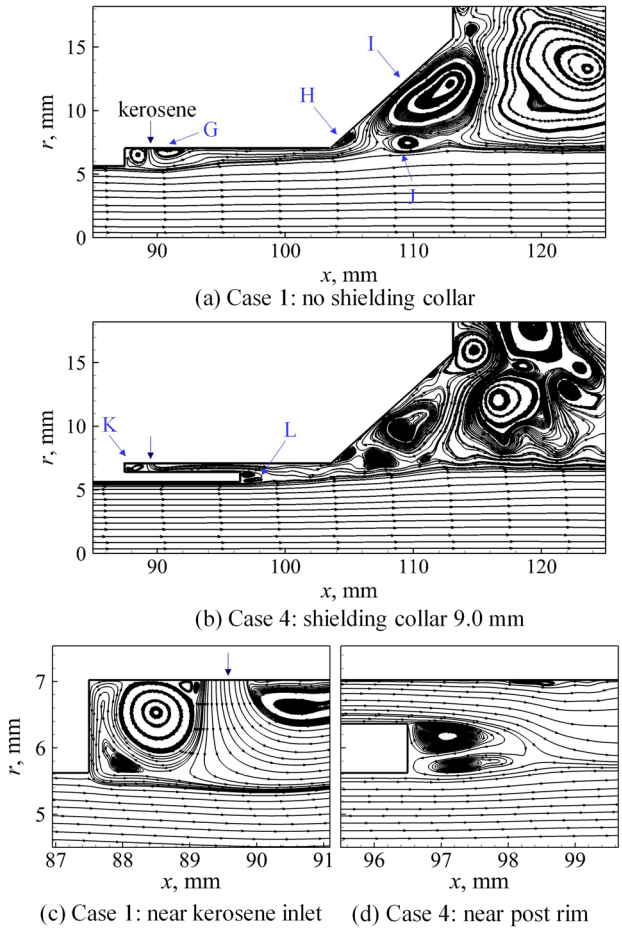

FIG. 14. Time-mean streamlines in the mixing section.

zone at the divergent point and a large recirculation zone in the downstream region. Secondary recirculation bubbles also appear.

In case 4, wavy streamlines visualize the unsteady kerosene flow in the fuel passage. A small recirculation bubble forms at the head end. As the kerosene and the GOX streams expand downstream of the post, two recirculation bubbles occur behind the shielding collar rim. Because of the limited recess length L_r, the near-wall streamlines originating in the kerosene stream are not flattened before the flow enters the taper region. A complicated vortical flowfield appears in the taper region, featuring multiple toroidal recirculation zones and secondary vortex structures.

Figure 15 shows the radial distributions of gauge pressure, kerosene mass fraction, and velocity components at five different axial locations in the time-averaged flowfield. The first axial location is 0.5 mm downstream of the GOX post end, $x = 88$ mm for case 1 and $x = 97$ mm for case 4. Case 1 has a slightly lower pressure and a larger axial velocity near the center. The pressure remains nearly uniform in the center region ($r < 5.4$ mm) and then increases continuously toward the wall at $r = 7.0$ mm, where the kerosene injection occurs. In the fuel passage ($r > 5.6$ mm), the axial velocity decreases substantially for both cases, while in case 1 the radial velocity increases up to 15 m/s. Within the post, case 1 has a negative radial velocity, suggesting a weak kerosene movement toward the GOX stream near the head end as observed in Fig. 14(c). In case 4, the recirculation zone downstream of the collar rim ($5.6 < r < 6.4$ mm) is characterized by a local pressure reduction, a negative axial velocity, and a wavy radial velocity profile.

The second axial location, $x = 103$ mm, is located 0.5 mm upstream of the entrance of the taper. In the kerosene/GOX mixing region ($r > 4.0$ mm), pressure and axial velocity decrease, while the radial velocity increases; this is especially noticeable in case 4. The third axial location, $x = 112$ mm, is located 1.1 mm ahead of the injector exit. As the flow expands in the taper region, pressure increases and axial velocity decreases. Kerosene spreads inward and reaches the radial location of $r = 2$ mm, as evidenced in the mass fraction profile; the small axial velocity and negative radial velocity mark the existence of a large recirculation flow in the kerosene plume. The fourth axial location, $x = 115$ mm, is located 1.9 mm downstream of the injector exit, where the flow expands rapidly. The GOX core shrinks and only covers the region of $r < 3$ mm, and kerosene spreads broadly, reaching the radial location $r > 20$ mm. The radial velocity is negative in the region of $5 < r < 15$ mm, under the influence of flow recirculation. At $x = 125$ mm, which is 11.9 mm downstream of the injector exit, the GOX core further decreases, as indicated by the weakened axial velocity in the region of $r > 2$ mm; the recirculating flow extends broadly, leading to a sizable radial velocity up to $r = 18$ mm in case 1 and $r = 22$ in case 4.

C. Mixing effectiveness

Figure 16 shows distributions of kerosene mass fraction in the time-averaged flowfield for all six cases. Also shown are the isolines of $\overline{y_F} = 0.2$, 0.4, 0.6, and 0.8. In cases 1 and 2, kerosene is well distributed in the taper region and near the injector exit. As the length of the fuel shielding collar increases

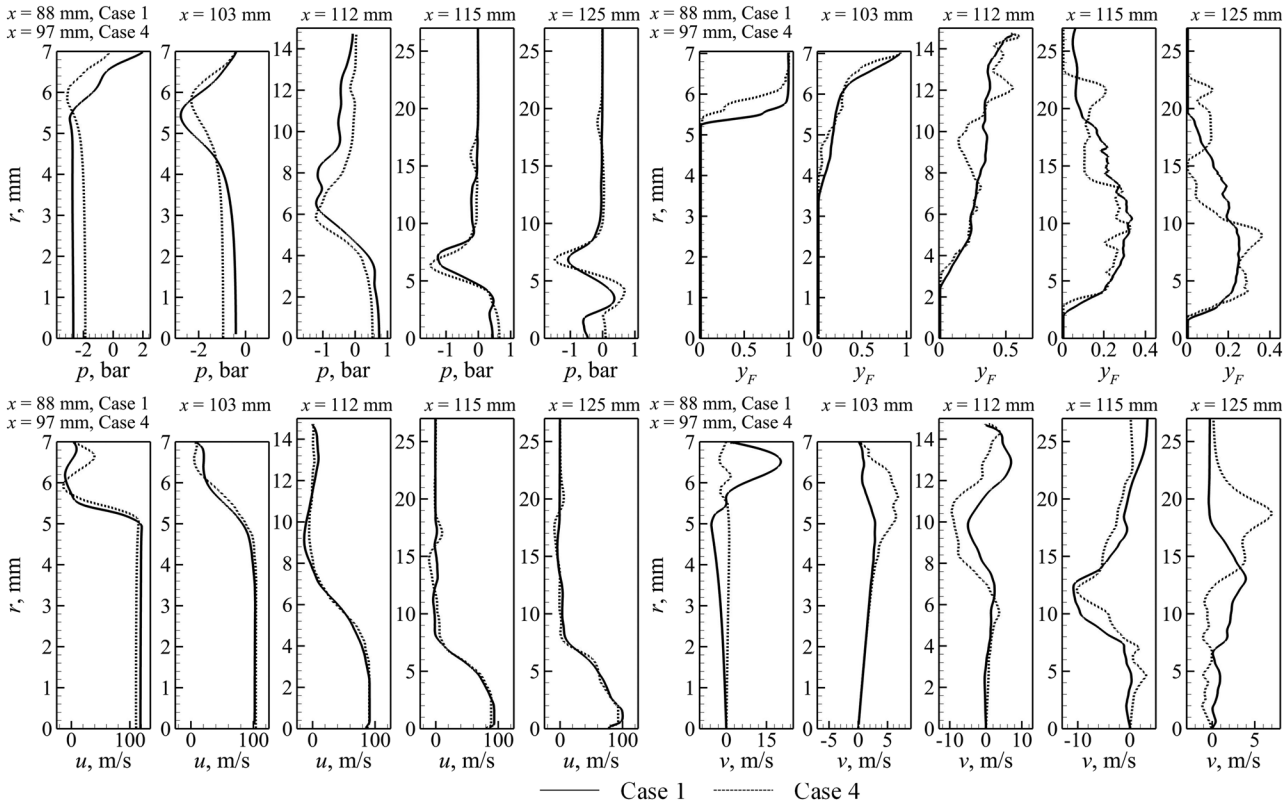

FIG. 15. Radial distributions of mean gauge pressure, kerosene mass fraction, and velocity components at different axial locations in the mixing section and initial chamber.

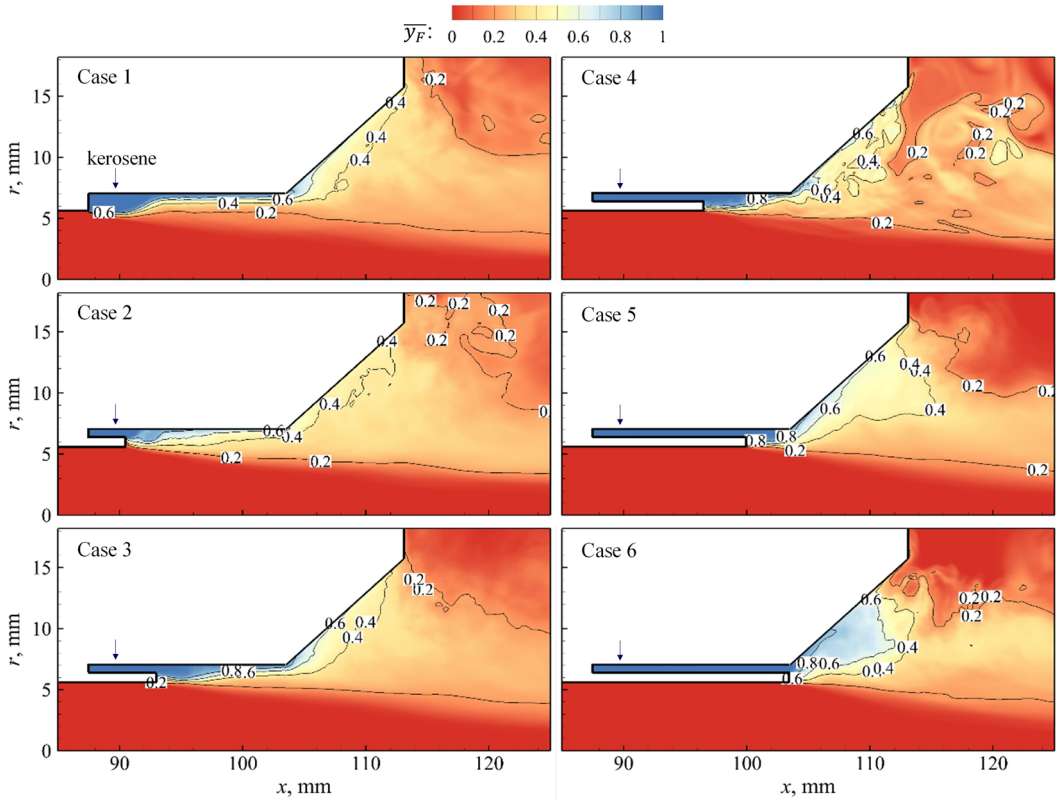

FIG. 16. Distributions of kerosene mass fraction in the time-mean flowfield (cases 1-6).

(the recess length decreases), the near-wall kerosene mass fraction increases and the plume shrinks, especially in cases 5 and 6.

To quantify mixing efficiency, the spatial mixing deficiency (SMD)[41] is calculated at several cross sections located between the GOX post end and the initial downstream region in the axial range of 88-145 mm. The SMD is a measure of spatial heterogeneity of flowfields and is calculated from the kerosene distribution over the cross sections of interest. The instantaneous kerosene mass fraction is denoted as $C_{i,k}$, where the subscript i ($i = 1, \ldots, m$) refers to the position and k ($k = 1, \ldots, n$) refers to the time instant. Over n snapshots, the SMD in a specified plane is calculated as

$$SMD = \frac{RMS_{plane}(\langle C_i \rangle)}{Avg_{plane}(\langle C \rangle)}, \tag{6}$$

where

$$\langle C_i \rangle = \frac{1}{n} \sum_{k=1}^{n} C_{i,k}, \tag{7}$$

$$RMS_i = \sqrt{\frac{1}{n-1} \sum_{k=1}^{n} (\langle C_i \rangle - C_{i,k})^2}, \tag{8}$$

$$Avg_{plane}(\langle C \rangle) = \frac{1}{m} \sum_{i=1}^{m} \langle C_i \rangle. \tag{9}$$

For all six cases, the calculations are performed in the regions of $0 \le R \le R_{\max}$, where $R_{\max}$ is the local radius of the injector and is selected to be 25 mm in the downstream region. Figure 17 shows the spatial evolution of SMD in percent for all six cases. The complex nature of the flow produces high spatial heterogeneity, as seen from the large values of SMD at the beginning of the mixing cup; these values only decrease in the taper region at around $x = 112$ mm and reverse in the downstream region. As the recess length decreases, an increasing trend in SMD occurs in the taper region, where nonuniform behaviors due to flow expansion and vortex amalgamation are observed. This is mainly attributed to the distance available for mixing layer development; a smaller SMD indicates a more homogeneous mixing field. In the downstream region, cases 3 and 4 show the lowest SMD, and cases 1 and 2 come second, a phenomenon related to the intrinsic flow development.

Overall, the unrecessed case 6 has the lowest mixing efficiency, primarily because of the absence of a mixing layer in the early mixing zone and the inherent flow structure behaviors of this injector design. The absence of a mixing layer means that disturbances in the later shear layers can feed back to the origin of the shear layer via the recirculation bubble, causing self-sustained oscillations that enhance the later mixing process.[43] The different stability behaviors have been observed by Juniper and Candel.[44] The wake-like behavior of a recessed coaxial injector was simulated by modeling a two-dimensional compound flow formed by a low-speed stream embedded

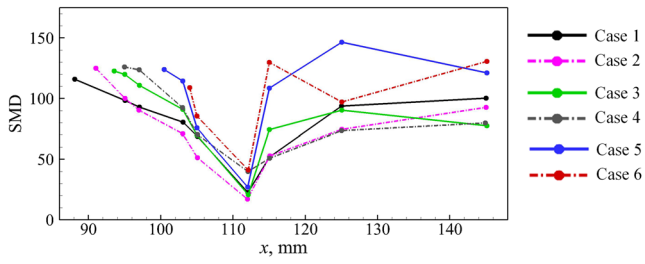

FIG. 17. SMD in the mixing zone (cases 1-6).

within a high-speed flow enclosed within a duct. It was found that the base of the recessed coaxial injector has a much larger absolutely unstable region than that of an unrecessed injector, and while the unrecessed injector is marginally globally stable, the recessed injector is globally unstable.

V. SUMMARY AND CONCLUSION

The present study treats supercritical fluid flow characteristics and mixing behaviors of gas-centered, liquid-swirl coaxial (GCLSC) injectors similar to those of the RD170/180 staged-combustion engines. Gaseous oxygen (GOX) and kerosene are used as the working fluids at a chamber pressure of 253.0 bars. The end of the center GOX post is recessed from the entrance of the taper region. Cases with different recess lengths (and correspondingly, fuel-shielding collar length) are studied to identify the influence of geometric attributes on the flow evolution and mixing.

Both instantaneous and time-averaged flow properties are examined systematically. In the case without the fuel-shielding collar, the initial kerosene/GOX interaction resembles a swirling transverse jet into a crossflow, and flow recirculation occurs near the kerosene injection slit and the head end. In other cases with the fuel-shielding collar, the kerosene flow is predominately axial before it enters the mixing zone; the coflow kerosene and GOX streams expand radially and form flow recirculation in the wake of the GOX post. Flow unsteadiness occurs during fluid injection and mixing. Vorticity production takes place in the boundary layer of the incoming GOX stream, along the wall of the fuel passage, and at the kerosene/GOX interface. As a result, the flowfield is characterized by salient vortical structures such as forward-rolling vortices whose sizes and spacing change as they convect downstream. Depending on the travel distance, as determined by the recess length, these vortices assume different levels of spatial coherence and macro-mixing capability that defines the early-stage mixing characteristics. As the flow enters the taper region, the vortices rapidly enlarge via stretching and/or amalgamation, changing the acoustic features and mixing effectiveness of the injectors. The flowfield is further complicated by another geometric change at the injector exit, and the downstream computational domain features multiple toroidal recirculation zones, flow separation, and reattachment, whose locations and structures vary according to the geometry.

Distributions of kerosene mass fraction are examined for all cases. Mixing efficiency is quantified according to the spatial mixing deficiency. Results show that as the recess length increases (the length of the fuel-shielding collar decreases), kerosene spreads more evenly and shows less spatial heterogeneity in the far downstream. This trend, however, does not apply at the injector exit, probably because of the different intrinsic flow instabilities associated with the specific design feature. This topic will be addressed in future work.

ACKNOWLEDGMENTS

This work was sponsored partly by the Air Force Office of Scientific Research under Grant No. FA 9550-10-1-0179 and partly by the William R. T. Oakes Endowment of the Georgia Institute of Technology. The authors gratefully acknowledge support and advice from Mitat A. Birkan.

[1] V. Yang, "Modeling of supercritical vaporization, mixing, and combustion processes in liquid-fueled propulsion systems," Proc. Combust. Inst. **28**, 925 (2000).
[2] J. C. Oefelein and V. Yang, "Modeling high-pressure mixing and combustion processes in liquid rocket engines," J. Propul. Power **14**, 843 (1998).
[3] H. Meng and V. Yang, "A unified treatment of general fluid thermodynamics and its application to a preconditioning scheme," J. Comput. Phys. **189**, 277 (2003).
[4] J. C. Oefelein, "Advances in the simulation of turbulent combustion," AIAA Paper 2015-1378, 2015.
[5] V. Bazarov, V. Yang, and P. Puri, "Design and dynamics of jet and swirl injectors," in *Liquid Rocket Thrust Chambers (Progress in Astronautics and Aeronautics): Aspects of Modeling, Analysis, and Design* (AIAA, 2004), Vol. 200, p. 19.
[6] D. Manski, C. Goertz, H.-D. Saßnick, J. R. Hulka, B. D. Goracke, and D. J. Levack, "Cycles for earth-to-orbit propulsion," J. Propul. Power **14**, 588 (1998).
[7] A. A. Vasin, S. D. Kamensky, B. I. Katorgin, A. I. Kolesnikov, V. P. Nosov, A. I. Stavrulov, V. V. Fedorov, and V. K. Chvanov, "Liquid-propellant rocket engine chamber and its casing," U.S. patent US6,244,041 B1 (June 12, 2001).
[8] M. L. Dranovsky, V. Yang, F. Culick, and D. G. Talley, *Combustion Instabilities in Liquid Rocket Engines: Testing and Development Practices in Russia*, Progress in Astronautics and Aeronautics Vol. 221 (AIAA, 2007).
[9] S. Soller, R. Wagner, H.-P. Kau, P. Martin, and C. Maeding, "Combustion stability characteristics of coax-swirl-injectors for oxygen/kerosene," AIAA Paper 2007-5563, 2007.
[10] K. Miller, J. Sisco, N. Nugent, and W. Anderson, "Combustion instability with a single-element swirl injector," J. Propul. Power **23**, 1102 (2007).
[11] M. D. A. Lightfoot, S. A. Schumaker, and S. A. Danczyk, "Atomization uniformity in gas-centered swirl-coaxial injectors," Report AFRL-RZ-ED-TP-2010-095, 2010.
[12] S. A. Schumaker, S. A. Danczyk, and M. D. Lightfoot, "Effect of cup length on film profiles in gas-centered swirl-coaxial injectors," AIAA Paper 2010-368, 2010.
[13] J.-H. Im, S. Cho, Y. Yoon, and I. Moon, "Comparative study of spray characteristics of gas-centered and liquid-centered swirl coaxial injectors," J. Propul. Power **26**, 1196 (2010).
[14] V. Kulkarni, D. Sivakumar, C. Oommen, and T. Tharakan, "Liquid sheet breakup in gas-centered swirl coaxial atomizers," J. Fluids Eng. **132**, 011303 (2010).
[15] J. Jeon, M. Hong, Y.-M. Han, and S. Y. Lee, "Experimental study on spray characteristics of gas-centered swirl coaxial injectors," J. Fluids Eng. **133**, 121303 (2011).
[16] S. A. Schumaker, S. A. Danczyk, and M. D. Lightfoot, "Effect of swirl on gas-centered swirl-coaxial injectors," AIAA Paper 2011-5621, 2011.
[17] N. Trask, D. P. Schmidt, M. Lightfoot, and S. Danczyk, "Compressible modeling of the internal flow in a gas-centered swirl-coaxial fuel injector," J. Propul. Power **28**, 685 (2012).
[18] J. G. Kim, Y. M. Han, H. S. Choi, and Y. Yoon, "Study on spray patterns of gas-centered swirl coaxial (GCSC) injectors in high pressure conditions," Aerosp. Sci. Technol. **27**, 171 (2013).
[19] J.-P. Matas, M. Hong, and A. Cartellier, "Stability of a swirled liquid film entrained by a fast gas stream," Phys. Fluids **26**, 042108 (2014).
[20] J. C. Sisco, Y. Yu, V. Sankaran, and W. E. Anderson, "Examination of mode shapes in an unstable model combustor," J. Sound Vib. **330**, 61 (2011).
[21] C. J. Morgan, K. J. Shipley, and W. E. Anderson, "Comparative evaluation between experiment and simulation for a transverse instability," J. Propul. Power **31**, 1696 (2015).
[22] G. Park, J. Lee, S. Oh, Y. Yoon, and C. H. Sohn, "Characteristics of gas-centered swirl coaxial injector with acoustic excitation of gas flow," AIAA J. **55**, 894 (2017).
[23] P.-G. Han, J. Seol, S. Hwang, and Y. Yoon, "The spray characteristics of swirl coaxial injectors," AIAA Paper 2003-0490, 2003.
[24] B.-D. Kim, S. D. Heister, and S. H. Collicott, "Three-dimensional flow simulations in the recessed region of a coaxial injector," J. Propul. Power **21**, 728 (2005).
[25] N. Zong, H. Meng, S.-Y. Hsieh, and V. Yang, "A numerical study of cryogenic fluid injection and mixing under supercritical conditions," Phys. Fluids **16**, 4248 (2004).

[26]G. Erlebacher, M. Y. Hussaini, C. G. Speziale, and T. A. Zang, "Toward the large-eddy simulation of compressible turbulent flows," J. Fluid Mech. **238**, 155 (1992).
[27]P. Dagaut, "On the kinetics of hydrocarbons oxidation from natural gas to kerosene and diesel fuel," Phys. Chem. Chem. Phys. **4**, 2079 (2002).
[28]N. Zong and V. Yang, "An efficient preconditioning scheme for real-fluid mixtures using primitive pressure–temperature variables," Int. J. Comput. Fluid Dyn. **21**, 217 (2007).
[29]H.-G. Li, N. Zong, X.-Y. Lu, and V. Yang, "A consistent characteristic boundary condition for general fluid mixture and its implementation in a preconditioning scheme," Adv. Appl. Math. Mech. **4**, 72 (2012).
[30]S.-Y. Hsieh and V. Yang, "A preconditioned flux-differencing scheme for chemically reacting flows at all Mach numbers," Int. J. Comput. Fluid Dyn. **8**, 31 (1997).
[31]R. C. Swanson and E. Turkel, "On central-difference and upwind schemes," J. Comput. Phys. **101**, 292 (1992).
[32]M. Sasaki, H. Sakamoto, M. Takahashi, T. Tomita, and H. Tamura, "Comparative study of recessed and non-recessed swirl coaxial injectors," AIAA Paper No. 97-2907, 1997, p. 2907.
[33]L.-J. Yang, M.-H. Ge, M.-Z. Zhang, Q.-F. Fu, and G.-B. Cai, "Spray characteristics of a recessed gas-liquid coaxial swirl injector," J. Propul. Power **24**, 1332 (2008).
[34]K. Ahn, Y.-M. Han, S. Seo, and H.-S. Choi, "Effects of injector recess and chamber pressure on combustion characteristics of liquid–liquid swirl coaxial injectors," Combust. Sci. Technol. **183**, 252 (2010).
[35]A. Mani, "Analysis and optimization of numerical sponge layers as a nonreflective boundary treatment," J. Comput. Phys. **231**, 704 (2012).
[36]H. Meng, G. Hsiao, V. Yang, and J. Shuen, "Transport and dynamics of liquid oxygen droplets in supercritical hydrogen streams," J. Fluid Mech. **527**, 115 (2005).
[37]N. Zong and V. Yang, "Cryogenic fluid dynamics of pressure swirl injectors at supercritical conditions," Phys. Fluids **20**, 056103 (2008).
[38]M. H. Yu and P. A. Monkewitz, "The effect of nonuniform density on the absolute instability of two-dimensional inertial jets and wakes," Phys. Fluids A **2**, 1175 (1990).
[39]G. L. Brown and A. Roshko, "On density effects and large structure in turbulent mixing layers," J. Fluid Mech. **64**, 775 (1974).
[40]L. Zhang, J. Y. Choi, and V. Yang, "Supersonic combustion and flame stabilization of coflow ethylene and air with splitter plate," J. Propul. Power **31**, 1242 (2015).
[41]L. Zhang and V. Yang, "Flow dynamics and mixing of a transverse jet in crossflow—Part I: Steady crossflow," J. Eng. Gas Turbines Power **139**, 082601 (2017).
[42]L. Zhang and V. Yang, "Flow dynamics and mixing of a transverse jet in crossflow—Part II: Oscillating crossflow," J. Eng. Gas Turbines Power **139**, 082602 (2017).
[43]H. Rehab, E. Villermaux, and E. Hopfinger, "Flow regimes of large-velocity-ratio coaxial jets," J. Fluid Mech. **345**, 357 (1997).
[44]M. P. Juniper and S. M. Candel, "The stability of ducted compound flows and consequences for the geometry of coaxial injectors," J. Fluid Mech. **482**, 257 (2003).